Canonical retinotopic shifts under an inverse force field explain predictive remapping

Ifedayo-EmmanuEL Adeyefa-Olasupo[1,2,3,*], Zixuan Xiao[4], & Anirvan S. Nandy[1,*]

1. Department of Neuroscience, Yale University
2. Department of Psychiatry, Charité - Universitätsmedizin Berlin
3. Berlin School of Mind and Brain, Humboldt-Universitat zu Berlin,
4. Department of Psychology, Beijing Normal University

*Corresponding authors (ifedayo-emmanuel.adeyefa-olasupo@charite.de , anirvan.nandy@yale.edu)

ABSTRACT

Saccadic eye-movements allow us to bring visual objects of interest to high-acuity central vision. Although saccades cause large displacements of retinal images, our percept of the visual world remains stable. Predictive remapping — the ability of cells in retinotopic brain areas to transiently exhibit spatio-temporal retinotopic shifts beyond the spatial extent of their classical receptive fields — has been proposed as a primary mechanism that mediates this seamless visual percept. Despite the well documented effects of predictive remapping, no study to date has been able to provide a mechanistic account of the neural computations and architecture that actively mediate this ubiquitous phenomenon. Borne out by the spatio-temporal dynamics of peri-saccadic sensitivity to probe stimuli in human subjects, we propose a novel neurobiologically inspired phenomenological model in which the underlying peri-saccadic attentional and oculomotor signals manifest as three temporally overlapping forces that act on retinotopic brain areas. These three forces – a compressive one toward the center of gaze, a convergent one toward the saccade target and a translational one parallel to the saccade trajectory – act in an inverse force field and specify the spatio-temporal window of predictive remapping of population receptive fields.

INTRODUCTION

In humans, the central 2° of visual space is extensively represented in the retina, superior colliculus, and the visual cortex and is therefore well suited for everyday tasks which require a detailed inspection of visual objects of interest. Saccadic eye-movements are recruited by the visual system to bring objects of interest that fall on the peripheral retina into the central 2° of visual space (i.e., foveate). Saccades cause large and rapid displacements of the retinal image. These displacements introduce significant disruptions, similar to those observed when attempting to photograph a rapidly moving object using a camera. However, the human visual system has evolved to account for these sudden image disruptions such that our perception of the visual scene remains relatively continuous and stable. The ability of the visual system to account for these disruptions is known as spatial constancy [1-6].

Translational remapping — the ability of cells in the superior colliculus, the frontal eye fields, the lateral intraparietal area, and extrastriate visual areas to predictively shift their sensitivity beyond the spatial extent of their receptive fields (RF) to their future post-saccadic locations— has been proposed as a primary mechanism that mediates this seamless visual percept [7-11]. However, more recent electrophysiological studies in the frontal eye fields and the extrastriate areas have challenged this dominant view of predictive remapping and have instead shown that receptive fields converge around a peripheral region of interest which includes the location of the saccade target. This form of predictive remapping is referred to as convergent remapping [12-13].

Translational and convergent accounts of remapping thus remain at odds, and the functional role that these divergent forms of transient RF shifts play in mediating spatial constancy remains unresolved. Further, no study to date has been able to uncover the behavioral correlates of pure convergent remapping [14]. Equally unresolved is the issue of time. A recent study has

reported that predictive remapping in visual area V4 includes a translational component followed by a convergent component [15], with each component occurring within distinct non-overlapping temporal windows [16]. This temporal account of predictive remapping is however at odds with the canonical order of pre-saccadic events [5] and a more recent study has challenged this result on methodological grounds [17].

In addition to these unresolved issues, there are three important issues pertaining to the visuo-motor system that have been previously overlooked. First, the frequency of saccades (~ 3-5 per second) [18] and the accompanied predictive receptive field shifts can be energetically expensive [19-20]. Yet the neural computations that balance energy costs with predictive function are unknown. Second, the neural architecture that supports neural sensitivity beyond the classic center-surround structure while preventing radical and unsustainable forms of remapping (e.g., over-convergence or over-translation) remains unexplored. Finally, no study has been able to uncover the mechanistic underpinnings that ensure the immediate availability of neural resources at the post-saccadic retinotopic location of the saccade target [21]. This immediate availability of neural resources cannot be explained by translational shifts towards the retinotopic cell's future field, or by the centripetal spreading of neural resources around the peripheral region of interest.

RESULTS

To provide an account for (a) the spatio-temporal characteristics that define predictive remapping, (b) the neural computations and architecture that ensure appropriate levels of peri-saccadic spatial sensitivity while preserving retinotopic organization, and (c) the immediate availability of neural resources towards the future center of gaze, we systematically assessed the transient consequences of predictive remapping on peri-saccadic sensitivity to visual probes along and around the path of

a saccade. Next, we investigated the rhythmicity that actively supported these changes across space and time. Finally, we proposed a novel neurobiologically inspired phenomenological model that succinctly capture the essence of our empirical observations.

Changes in peri-saccadic sensitivity reflect active extraretinal mechanisms that aligns with the spatio-temporal attributes of canonical pre-saccadic events

We assessed changes in peri-saccadic sensitivity across visual space using a cued saccade task (Fig 1). We specifically examined changes in peri-saccadic sensitivity at points along the saccade trajectory ('radial axis') and at points orthogonal to the saccade trajectory ('tangential axis'), while subjects fixated, planned, and executed a saccadic eye-movement toward the saccade target. We probed specific radial points at foveal ($rad_{fov-out}$, rad_{fov-in}), parafoveal ($rad_{para-in}$, $rad_{para-out}$) and peripheral ($rad_{peri-in}$, $rad_{peri-out}$) locations, and tangential points symmetric to one another with respect to the radial axis at foveal ($tan_{fov-ccw}$, tan_{fov-cw}), parafoveal ($tan_{para-ccw}$, $tan_{para-cw}$) and peripheral ($tan_{peri-ccw}$, $tan_{peri-cw}$) locations, before and after the central movement cue. In each trial, a low contrast probe was flashed at one of these locations (chosen at random) for 20ms with 75% probability; in 25% of trials (control trials) no probe was flashed. The contrast of the probe stimuli was chosen (independently for each subject and for each spatial location cluster; see Methods) such that detection probability was at 50% in the absence of eye movements. The probes were presented at a random time from 600ms before to 360ms after the central movement cue. Our design thus allowed us to measure peri-saccadic sensitivity along and around the entire saccade trajectory, and at a fine temporal scale.

Subjects reported whether they were able to detect the flashed probe using a push button. The control (no probe) trials allowed us to assess the incidences of false alarms. Low false alarm

rates of 1.2%, 1.4% and 1% (along the radial, tangential counterclockwise and clockwise axes respectively) gave us high confidence about subjects' peri-saccadic sensitivity reports. We collected ~ 21,000 trials, with a minimum of 1,500 trials per subject. Control trials were excluded from our main analyses. We plotted the normalized average peri-saccadic sensitivity of eleven subjects as a function of flashed probe times relative to saccade onset, at spatially overlapping ($rad_{fov+para-in}$, $rad_{para+peri-in}$) and non-overlapping ($rad_{fov-out}$, $rad_{peri-out}$) points along the radial axis and symmetric points ($tan_{fov-ccw+cw}$, $tan_{para-ccw+cw}$, $tan_{peri-ccw+cw}$) along the tangential axis (Fig 2A). Corresponding error estimates were obtained using a 20-fold jackknife procedure in which the sensitivity was estimated from 95% of the data (see Methods).

We found a graded profile of sensitivity along the radial axis in the time period 540ms to 240ms before saccade onset: an immediate and sharp decline in peri-saccadic sensitivity in the outer peripheral region ($rad_{peri-out}$), a modest decline in peri-saccadic sensitivity at the outer parafoveal region ($rad_{para+peri-in}$), and sustained levels of peri-saccadic sensitivity in the foveal ($rad_{fov-out}$) and inner parafoveal ($rad_{fov+para-in}$) regions. (Fig 2a, left panel). This is in alignment with prior reports of peri-saccadic compression of visual space toward the fovea as subjects maintain fixation prior to the deployment of attention towards the periphery [22-24]. This was followed by a modest rebound in peri-saccadic sensitivity at the more eccentric locations ($rad_{peri-out}$ and $rad_{para+peri-in}$) from 240ms to 130ms prior to saccade onset, consistent with a pre-saccadic shift of attention toward the saccade target [5-6, 12-13, 17]. From 130ms to around 60ms before saccade onset, we found expected declines in peri-saccadic sensitivity across retinotopic locations. This global decline in peri-saccadic sensitivity is in agreement with peri-saccadic corollary discharge commands originating from pre-motor brain areas as well as with visual-transient signals originating from the retina to retinotopic brain areas just before subjects

executed a saccade [25-29]. Shortly after the execution of a saccade, we found an immediate increase in peri-saccadic sensitivity in the outer parafoveal and peripheral regions, while continual declines in peri-saccadic sensitivity, as we had expected, was found in the fovea and inner parafoveal regions. For the symmetric retinotopic locations along the tangential axes, we found around 540ms to 240ms before saccade onset a delayed decrease in peri-saccadic sensitivity in the peripheral region ($tan_{peri-ccw+cw}$), along with either a modest increase in peri-saccadic sensitivity in the parafoveal region ($tan_{para-ccw+cw}$) or sustained levels of sensitivity in the foveal ($tan_{fov-ccw+cw}$) region (Fig 2A, right panel). Similar to the radial axis, peri-saccadic sensitivity at the peripheral region showed a modest rebound from the period 240ms to 130ms prior to saccade onset, followed by a global decline in sensitivity at all locations. During the period immediately after saccade onset, we found a larger and immediate increase in peri-saccadic sensitivity at the outer parafoveal and peripheral regions, along with continual declines at the foveal region [21].

Delta and theta- rhythmicity known to support attentional shifts during visual search and the reorientation of attention across visual space mediates peri-saccadic sensitivity.

Our behavioral results suggest that peri-saccadic sensitivity is much more dynamic than previously reported. We hypothesized that these dynamics are a consequence of pre-saccadic attentional shifts [30]. To test this, we assessed the spectral signature of the observed changes in visual sensitivity. The logic behind this assessment is as follows: if these changes are a consequence of attentional shifts, then the spectral signature associated with these changes should resemble, if not match, known rhythmic patterns of attentional shifts. Conversely, if the spectral architecture we find fails to recapitulate these known rhythmic patterns, then these changes cannot be directly attributed to attentional shifts.

To calculate the spectral amplitude that underlie these changes in visual sensitivity in the foveal, parafoveal and peripheral regions of the visual field, we transformed each subject's detrended raw time-series sensitivity data into the frequency domain using the Fast Fourier transform (FFT) (Supplementary Fig 1A-B). The mean FFT and corresponding standard error of mean across subjects was subsequently obtained for each region (See Methods).

Peri-saccadic sensitivity at the less eccentric ("foveal") locations ($rad_{fov-out}$, $rad_{fov+para-in}$, $tan_{fov-ccw+cw}$) exhibited rhythmicity in the delta frequency band at ~3 Hz (Fig 2B, left panel). In line with our hypothesis, this rhythmic pattern is known to support peri-saccadic attentional shifts that mediate visual sensitivity at suprathreshold levels [31-33]. We also found secondary peaks at ~5 Hz (theta-band). This rhythmic pattern is known to support the reorientation of visual attention towards different regions of visual space during visual search [34-37]. Spectral differences calculated using location shuffled data (n=1000) versus the non-shuffled data were not statistically significant (two tailed paired-sample t-test) suggesting that the peri-saccadic rhythmicity in the foveal region is not location specific (Fig 2C, left panel).

At the more eccentric ("parafoveal" and "peripheral") locations ($tan_{para-ccw+cw}$, $tan_{peri-ccw+cw}$, $rad_{para+peri-in}$ $rad_{peri-out}$), we found that sensitivity also exhibited delta-band rhythmicity (Fig 2B, right panel). With the exception of the symmetric tangential points in the parafoveal locations ($tan_{para-ccw+cw}$), no secondary theta-band peaks were found. Importantly, spectral differences between the shuffled and non-shuffled data sets were significantly different at the $rad_{para+peri-in}$ and $rad_{peri-out}$ locations (p=0.0276, p=0.0368, two tailed paired-sample t-test). These differences suggest that peri-saccadic rhythmicity around the saccade target location is indeed location specific (Fig 2C, middle panel).

Eccentricity dependent low-frequency power supports early and later attentional shifts across visual space

Our frequency result provide evidence that changes in peri-saccadic visual sensitivity are the consequence of distinct attentional shifts that are supported by low-frequency delta- and theta-band fluctuations. Our results also show that these rhythmic sensitivity patterns are spatially selective in the periphery, specifically along the radial axis around the saccade target. Next, we assessed the temporal dynamics associated with these peri-saccadic rhythmic patterns by calculating the time-frequency spectrograms at each spatial location (Fig 3A, B; see Methods). Visual attention shift is known to occur before the planning and preparation of the impending saccade which takes places at ~150 to 200ms before saccade onset [38-39]. Assuming visual attention shifts from less eccentric (foveal) to the more eccentric (parafoveal and peripheral) regions of the visual field, we might expect these shifts to be accompanied by progressively delayed increases in low-frequency (3-5 Hz) power from the foveal region to the peripheral regions.

We estimated the onset time of increases in low-frequency power for each location along and around the saccade trajectory (see Methods). Onset time of low-frequency power as a function of eccentricity (Fig 3C) reveals two general temporal patterns. First, the more foveal retinotopic locations exhibit early increases in low-frequency power followed by delayed increases in low-frequency power at the more eccentric retinotopic locations. This suggests that the onset of these increases in low-frequency power is eccentricity dependent. It is important to note that the observed increases in low-frequency power at all locations happen well before saccade preparation time. These results further suggest that there are likely two distinct attentional shifts meditating peri-saccadic sensitivity across visual space: an early shift towards the fovea and a later shift

towards the periphery. Second, we see a temporally overlapping increase in low-frequency power at all peripheral locations around the saccade target. Coupled with the immediate availability of post-saccadic sensitivity at these locations (Fig 2A), this suggests that cells in retinotopic brain areas transiently exhibit spatio-temporal retinotopic shifts not only towards their future fields but also around the saccade target and at the future center of gaze.

Novel neurobiologically inspired phenomenological model

Population receptive fields (pRFs) across retinotopic brain areas are not static but can exhibit transient spatial shifts [7-17]. To this end, we developed a simple yet powerful novel neurobiologically inspired phenomenological model that allows the pRFs of cells in retinotopic brain areas to transiently undergo spatio-temporal retinotopic shifts beyond the spatial extent of their classical receptive fields consistent with translational, convergent as well as other biologically plausible forms of remapping.

Our model assumes that there are limits to the extent of these transient retinotopic shifts such that retinotopic organization is always maintained [40]. Consequently, within our model we extend the concept of a cell's receptive field by introducing its elastic field. Population elastic fields (pEFs) constitute the spatial limits within which pRFs are allowed to transiently shift. These transient spatial shifts manifest as contortions of pRF shape (e.g., shrinks or stretches) [12, 17, 41] and temporarily distort the representation of visual space [24, 42, 43]. pEFs span the region immediately beyond the classical extent of the pRF, their spatial extent is proportional to the eccentricity of the classical pRF and they are omnidirectional with respect to the classical pRF (Fig 4A).

Visually transient signals originating from the retina and corollary discharge signals originating from pre-motor brain structures are sent to relevant retinotopic brain areas [28-32]. At its core, our model assumes that these salient visuo-motor signals act as forces that perturb pRFs from their equilibrium positions. We model these forces as being exerted by corresponding time varying masses (M) in a "retinotopic force field". The perturbations due to these forces are limited to the spatial extent of pEFs and are inversely proportional to the distance between the pRF and M (Fig 4A, right panel). These principles ensure that pRFs are appropriately sensitized around the loci of task-relevant salient cues while minimizing the energy cost associated with spatial perturbations.

Prior to a saccadic eye-movement, visuo-motor signals arrive faster at the fovea in the direction of the more eccentric region where the saccade target resides [44]. Therefore, both the current center of gaze and the path to the saccade target inherently benefit from earlier and faster visual processing, reflecting a detailed visual representation within these retinotopic regions [22]. Conversely, at the more eccentric parts of the visual field, visual processing is slower and yields a more diffuse visual representation within these retinotopic regions [43-45]. In light of these previous results and our own observations that the onsets of peri-saccadic sensitivity were eccentricity dependent, with progressively delayed increases in low-frequency (3-5Hz) power from the foveal region to the peripheral regions (Fig 3), we posit that pre-saccadic attentional and oculomotor processes manifest in three predictive forces that aligns with the spatio-temporal attributes of canonical pre-saccadic events [5] and impinge on the retinotopic visual cortex (Fig 4B, left panel). We predict that these interactions should lead to transient perturbations of pRFs in accordance with the principles described above and are the underlying causes of predictive remapping (Fig 4B, right panel).

The earliest – a compressive force, overlapping with the time of fixation, causes pRFs to transiently exhibit compressive shifts towards the current center of gaze. We predict that these compressive shifts facilitate the acquisition and storage of information and resources the visual system will eventually transfer towards the predicted future center of gaze [46-47]. The compressive force is followed by a convergent force, which align with the deployment of attention towards the peripheral target and causes pRFs to transiently exhibit convergent shifts around the peripheral site [12,13]. This convergence provides a perceptual advantage around the task-relevant target [5, 44]. Finally, as the organism prepares and plans to execute the imminent saccadic eye-movement, a translational force causes pRFs to shift towards their future receptive fields [7-11]. This, in combination with a declining compressive force, ensure a handoff of neural resources toward the future center of gaze [21].

Spatio-temporal retinotopic shifts under an inverse-distance rule, aligns with the predictions proposed by early neurophysiological studies

The underlying retinotopic architecture of our model was composed of retinotopic population receptive fields (pRFs) that tile visual space, with their size being proportional to their eccentricity. The population elastic fields (pEFs) of pRFs were also proportional to their eccentricity. We introduced three canonically ordered external independent forces, which for the reasons we have highlighted above is consistent with an inverse-distance rule (see Supplementary Fig 2A-D). The peri-saccadic perturbation of pRFs produced peri-saccadic spatiotemporal retinotopic shifts within pEFs (Fig 4C, Supplementary Fig 3A-F) which manifested in time-varying modulation of density read-outs, equivalent to changes in visual sensitivity in our psychophysical experiments (See Methods). Remarkably, we found that each independent force was able to recapitulate specific

aspects of peri-saccadic sensitivity. When modelled pRFs were perturbed by a declining central force, we found a hand-off in density levels between the $rad_{para+peri-in}$ and $rad_{peri-out}$ locations (Fig 5A, left panel). This result, in part, strongly resembles the immediate availability of peri-saccadic sensitivity at the approximated future center of gaze in the periphery, which points to the role of the central force in meditating sensitivity at these locations. Under the perturbation by a peripheral force alone, we found sustained density levels at the $rad_{fov-out}$ and $rad_{para+peri-in}$ locations (Fig 5A, middle panel), in contrast to a modest increase in density at the $rad_{fov+para-in}$ location, and a large decline in density level at the $rad_{peri-out}$ locations. This result is the direct consequence of retinotopic shifts converging towards the peripheral target. Finally, under a translational force alone, we found sustained levels in density at less eccentric retinotopic locations, while at the more eccentric retinotopic locations we found modest declines in density levels (Fig 5A, right panel). As the force was withdrawn, we found a hand-off in density levels between the most eccentric locations, although this was weaker than that observed for the central force.

Spatio-temporal retinotopic shifts under an inverse-distance rule explains peri-saccadic sensitivity across visual space.

While each independent force was able to recapitulate specific aspects of peri-saccadic dynamics, we next systematically explored the extent to which combinations of these forces could explain our empirical observations. When modelled pRFs were perturbed by the combination of a central and peripheral force (Fig 5B, left panel), we found relatively sustained levels in density except for $rad_{peri-out}$. As the influence of the peripheral force declined, we found a steady decline in density at the less eccentric retinotopic locations and steady increase at the more eccentric retinotopic

locations, largely recapitulating our empirically observed changes in sensitivity just prior to saccade execution (Fig 2A, left panel). Under the perturbation by the combination of a central and translational force (Fig 5B, middle panel), we found a large and immediate increase in density levels around the future center of gaze in the periphery. Under the perturbation by the combination of convergent and translational forces (Fig 5B, right panel), we found distinguishable differences in density between the less eccentric versus the more eccentric retinotopic locations.

Finally, when modelled pRFs were perturbed by a combination of all three independent forces (Fig 5C, left panel), as we had expected, the initial changes in density were similar to those observed under the combination of a central and peripheral force (Fig 5B, left panel). Shortly after the introduction of the translational force, we found rapid declines in sensitivity at less eccentric locations, in contrast to a rebound in sensitivity at the more eccentric locations. Quite convincingly, the combination of these three independent forces recapitulates our empirical observations. Note that the perturbation of pRFs without their pEFs failed to recapitulate our empirical observations due to an over compression towards the fovea (Fig 5C, right panel). This result points to the importance of pEFs in ensuring that appropriate levels of peri-saccadic spatial sensitivity is allocated while preserving retinotopic organization.

DISCUSSION

Our study was motivated by what is arguably the most puzzling question in the field of predictive remapping research. In 1990 Goldberg and Bruce recapitulated translational effects observed in the superior colliculus by Mays and Sparks ten years earlier [48]. They found that before the execution of a saccade, the receptive fields of cells in the frontal eye fields predictively shift their spatial extent beyond their classical extent towards their future fields (translational remapping)

[49]. These neural effects were reproduced across several retinotopic brain areas including the lateral intraparietal area [7] and extrastriate visual areas [11]. About two decades later, recapitulating in part the results of Tolias and colleagues [12], Zirnsak et al. demonstrated that the receptive fields of cells in the frontal eye fields primarily converge around the attention-selected peripheral region of interest which included the spatial extent of the saccade target (convergent remapping) [13]. We revisited these contradictory findings from a functional perspective by systematically assessing the transient consequences of retinotopic remapping on peri-saccadic sensitivity along and around the path of a saccade. We then introduced a novel neurobiologically inspired phenomenological model in which we proposed that the underlying peri-saccadic attentional and oculomotor signals manifest as temporally overlapping forces that act on retinotopic brain areas. We show that, contrary to the dominant spatial account [7-11, 14, 50-51], predictive remapping is not a purely translational phenomenon but rather one which fundamentally includes a convergent [12,13, 52] and a compressive component (Fig 2A, left panel and Fig 5C, left panel). We also demonstrate that, contrary to the dominant temporal account of predictive remapping [15-16], compressive shifts towards the fovea precede and overlap with convergent shifts towards the peripheral region of interest, while translational shifts parallel to the saccade trajectory occurs later in time [17] and overlap with convergent shifts.

Our study makes four principal contributions to a deeper understanding of predictive remapping. First, recipient retinotopic brain areas receive temporally overlapping inputs that align with a canonical order of pre-saccadic events (Fig 4). Second, the neural computations that underlie predictive remapping, obeys an inverse distance rule (Supplementary Fig 2). Third, during an active state (when not in a state of equilibrium) pRFs very likely possess putative transient pEFs which allows retinotopic receptive fields to undergo a remarkable degree of elasticity beyond their

classical spatial extent. In fact, as our simulation results show, in the absence of these pEFs our perception of the visual world would be dramatically distorted, as retinotopic cells would over-commit to certain loci in visual space at the expense of others (see Fig 5C, middle panel). Finally, our study strongly suggests that the immediate availability of neural resources after the execution of the saccade is uniquely mediated by previously compressed neural resources at the current center of gaze (Fig 4A, left panel, Fig 4B, left and middle panels, Fig 4C, left panel). Indeed, without compressive signals or pEFs, attentional resources that are needed at the approximated location of the target would be significantly delayed and in the extreme case non-existent (Figure 4A, middle panel, Figure 4B, right panel, Figure 4C, middle panel).

The reason why the $rad_{peri-out}$ location in the periphery demonstrated the largest and most rapid increase in peri-saccadic resources just before the eye was set to land is a curious point (Supplementary Fig 1C). One possibility is that the representation of the peripheral target does not always match the location it is objectively subtended at [24, 42, 43], and thus in the case of our experiment the target appeared slightly mis-localized in the direction of the $rad_{peri-out}$ location. However, a more likely explanation is that this location significantly contributed to the net neural resource allocated towards the current center of gaze when attention was initially deployed towards that locus (Fig2A, left panel). Consequently, once resources were being deployed towards the approximated future center of gaze, around the time subjects began to plan and prepare to make a saccade, the delivery of resources at this peripheral site was larger and much more rapid than any other retinotopic location in the periphery.

In conclusion, our study provides a mechanistic account of the neural computations and architecture that mediates predictive remapping which had eluded the field for decades and provides critical insights that will inform future neural investigations of this phenomenon.

FIGURE CAPTIONS

Figure 1. Peri-saccadic probe-detection task.

(A) Spatial locations tested across experiments. Colored circles show the locations at which a low-contrast probe was flashed as subjects planned and prepared a saccade (black arrow) towards the periphery. Probe locations are shown only for horizontal saccades to the right. For other saccade target locations, the probe locations were appropriately positioned along and around the path of a saccade. In the foveal and parafoveal experiments, a saccade target (gray or red asterisk) was presented at azimuth angles of 0°, 45°, 315° (each subject had a different angle). In the peripheral experiment the saccade target was presented either at azimuth angles of 0°, 45°, 90°, 270°, 315° (each subject had a different angle).

(**B**) Temporal sequence of an example trial. The start of a trial began with the appearance of a fixation point, followed by a time-varying presentation of the saccade target. A low-contrast probe was flashed either before the onset of the central movement cue (the pre-saccadic condition), or after (the post-saccadic condition).

Figure 2. Peri-saccadic sensitivity functions and their frequency domain representation across visual space.

(**A**) Thick solid lines represent normalized changes in peri-saccadic sensitivity as a function of flashed probe times relative to saccade onset along and around the saccade trajectory (n=11). The thin lines represent corresponding error estimates obtained using a 20-fold jackknife procedure in which the sensitivity was estimated from 95% of the data.

(**B**) Frequency domain representation of detrended peri-saccadic sensitivity. The thinner solid lines represent the error estimates calculated across subjects.

(**C**) Frequency domain representation of shuffled peri-saccadic sensitivity data (n=1000).

Figure 3. Time-frequency spectrograms across visual space during peri-saccadic probe-detection task.

(A) Time-frequency spectrogram at the less eccentric (foveal) locations. The vertical solid lines represent onset of increase in low-frequency power, while the vertical dashed lines represent the error estimates. The solid horizontal lines represent the low-frequency power range from 3 to 5 Hz.

(**B**) Same as in (A) at the more eccentric (parafoveal and peripheral) locations.

(**C**) Estimation of onsets of increases in low-frequency power around and along the path of a saccade. Onset estimates were fitted with a linear regression line. Onset time increased as the spatial location being sampled became more eccentric. Error bars indicate standard error of the mean.

Figure 4. Retinotopic force field of predictive remapping.

(A) Retinotopic field consisting of population receptive field (pRFs) that tile visual space. For illustration purposes, a single pRF is highlighted in orange. This pRF is characterized by the location of its center at equilibrium (gray dot), its size (orange circle) and a movement extent (elastic field, pEF; dashed orange circle). Both pRF size and pEF extent are eccentricity dependent. M_C represents compressive signals and is modelled as a varying mass located at the center of gaze. M_P represents convergent signals and is modeled as a varying mass located at the peripheral site

corresponding to the saccade target. M_T represents translational signals and is modelled as a virtual mass at infinity located in the direction of the impending saccade.

(B) Temporally overlapping varying masses for the case when pRFs were perturbed by a combination of all three independent forces.

(C) Corresponding spatiotemporal pRF trajectories under an inverse force field ($\alpha = -1.1$). Note that each pRF possess an eccentricity dependent pEF, however for illustration purposes only a few are shown (black circles). The trajectories are color coded as in (B).

Figure 5. Temporally overlapping compressive, convergent and translational shifts explain peri-saccadic changes in sensitivity across visual space. Simulation results at $\alpha = -1.1$ in cases when pRFs are perturbed by (**A**) a single external force (**B**) two external forces and (**C**) three external forces. The right panel in (**C**) are the results for the three force simulations without elastic fields. Along the right y axis is the magnitude of the time varying masses used to model putative signals to the retinotopic field, while the x-axis represents the simulation time sampled at discrete increments of 1ms.

Supplementary Fig. 1. Raw, detrended and normalized peri-saccadic sensitivity

(**A**) Raw sensitivity along the radial axis (left panel) and the tangential axes (right panel).

(**B**) Detrended sensitivity along the radial axis (left panel) and the tangential axes (right panel).

(**C**) Normalized peri-saccadic sensitivity in the periphery.

Supplementary Fig. 2. Simulation results for α values ranging from -1.5 to 1.5. On the x-axis is the simulation time sampled at discrete time increments of 1ms. Along the left y axis is

normalized density at one of the four radial locations: $rad_{fov-out}$, $rad_{fov+para-in}$, $rad_{para+peri-in}$, $rad_{peri-out}$. Along the right y axis is the magnitude of the time varying masses used to model putative signals to the retinotopic field. Alpha values consistent with inverse-distance rule (-1.5 to 0) is represented in an orange-gray gradient, while alpha values consistent with proportional-distance rule (i.e., 0 to 1.5) is represented in a blue-gray gradient. Simulation results for pRFs perturbed by **(A)** a translational force, **(B)** translational and peripheral forces, and (**C**) central, peripheral, and translational forces.

Supplementary Fig. 3. Spatiotemporal pRF shifts during different stimulations. Retinotopic shifts produced by the perturbation of pRFs (**A**) under a central force alone, (**B**) peripheral force alone, (**C**) translational force alone, (**D**) central and peripheral forces, (**E**) central and translational forces, and (**F**) peripheral and translational forces. Same conventions as in Figure 4C.

ACKNOWLEDGEMENTS

This research was supported by NARSAD Young Investigator Grant, Ziegler Foundation Grant, Yale Orthwein Scholar Funds and Lawrence Family Young Investigator Award to ASN, and by NEI core grant for vision research P30 EY026878 to Yale University. We would like to thank Barbora Wichterlová for reading multiple edits of the manuscript. We would also like to thank Alec Sheffield and Olivia Meisner for their helpful comments on the manuscript.

AUTHOR CONTRIBUTIONS

ASN & EL conceptualized the project. ASN supervised the project. EL collected the data. EL & XZ preprocessed the behavioral data. EL analyzed the behavioral data. EL & ASN developed the

computational model. EL implemented the model and performed the model simulations. EL & ASN wrote the manuscript.

COMPETING INTERESTS

The authors declare no competing interests.

METHODS

Predictive Remapping Experiment

Consenting human subjects. Eight subjects, all with corrected-to-normal visual acuity, provided written and informed consent prior to the study. Each subject, with the exception of two individuals (both authors), were compensated 20 USD per hour for their participation. The protocol for this study, the collection and storage of the data was approved by the Yale Ethic Review board and was in accordance with the Declaration of Helsinki.

Viewing distance. Subjects sat comfortably with their chin and forehead placed against a custom-built head support apparatus consisting of an adjustable chin rest, forehead support and a bite bar holder. The center of the experimental display was placed at a distance of 57cm from the eye. In order to ensure tight control over viewing distance and eye-position, subjects placed a bite bar (personalized deep-impression dental bite-bar) inside their mouth. The bite bar was then affixed to the head support apparatus for the duration of the experimental session.

Stimulus and presentation. Visual stimuli were presented on a gamma corrected LCD monitor using custom-designed Window software (Picto). All stimuli presented in the control and main

experimental sessions, with the exception of the achromatic Gabor probes (0.5 degrees of visual angle [dva], 0° orientation, $\pi/2$ phase), were constructed in Picto. The display was driven by a NVIDIA graphics card with a color resolution of 8 bits per channel. Its spatial resolution was 1400 × 1050 pixels with a refresh rate of 85 Hz (11.76 ms per frame), and an average mean luminance of 38 cd/m^2.

Eye-movement Tracking. The right eye (the dominant eye for all subjects) was tracked using an infrared video-based eye-tracker sampled at 1kHz (I-Scan Inc., Woburn, MA). At the beginning of each experimental session, we performed a custom-developed 9-point eye-calibration procedure in Picto. This procedure allowed for the correction of any drift in gaze at the onset of a trial. Overall, the gaze error within subjects varied from 0.25° to 1.0° with an average gaze error of 0.45° across subjects.

Contrast Sensitivity Function measurement. Prior to the main task, we measured the Contrast Sensitivity Function (CSF) at an eccentricity corresponding to the mean location at which probes were presented for the main task. CSF was measured using a set of Gabor stimuli contrasted against a gray background with 21 contrast levels ranging from 1 to 55%. At the onset of each trial, subjects were instructed to acquire and maintain fixation for at least 1000ms. Trails were aborted if the eye-position deviated from fixation by more than 1 dva. A Gabor stimulus with a randomly selected contrast level was then flashed for 20ms. Subjects had to indicate with a button-press whether they were able to detect the stimulus. Each contrast level was presented 10 times, along with a non-probe condition, which controlled for any potential false alarms. After the conclusion of this session, a logistic function was used to estimate a psychometric curve fitted to the data to compute a CSF. The contrast at which the subject could detect the stimuli with 50% accuracy was

chosen as the probe contrast level for the main task. The CSF measurement sessions lasted approximately 70 minutes.

Cued saccade task. In the main experiment, subjects performed a cued saccade task (Fig 1A). Before the commencement of an experimental session, each subject took ~15 minutes to adapt to the scotopic condition in the experimental room. At this time, a 9-point eye-position calibration procedure was performed (see above). Subjects initiated a trial by maintain gaze on a central fixation dot (subtending 0.5 dva in diameter) for 300ms. If the eye deviated from this dot by more than 1 dva, the trial was aborted. After a variable delay period of 0-300ms a saccade target (white circle) appeared at a 10° eccentric location (Fig 1A). Subjects were required to maintain fixation for another 300-600ms, at the end of which the fixation dot was extinguished, which served as the central movement cue to make a saccade towards the saccade target (Go_{onset}, Fig 1B). The saccade target remained on the display for another 500ms after the central movement cue. A 2-dva radius tolerance window around the saccade target was used to detect whether the saccade landed on the target within this 500ms window. Subjects were provided visual feedback about the outcome of the trial by changing the color of the saccade target to green for a correct saccade landing within the tolerance window or red for saccades landing outside the tolerance window. On 25% of the trials a Gabor probe (contrast set to 50% detection rate from the CSF measurement), was flashed for 20ms at a random time during the 300-600ms window between the onset of the saccade target and the central movement cue. On 50% of the trials, the probe was presented at a random time between 0-340ms after the central movement cue. To control for any false alarms no probe was flashed in the remaining 25% of trials. These three conditions were randomly interleaved across trials. Subjects indicated whether they detected the probe by a button press. Consecutive trials were

separated by a 1000ms inter-trial interval. The spatial locations of the flashed probes depended on the experimental conditions outlined below. Each experimental session lasted about 70 minutes with a 10-minute break in the middle. Subjects took about 3 weeks to complete the main experiment.

Foveal probes condition. 3 subjects (all female, M_{age}= 22, SD =1.7) were recruited for the foveal condition. With the exception of subject XZ (s_{XZ}, an author), each subject was completely naïve to the aim of the experiment. Saccade targets appeared at an eccentricity of 10° and at azimuth angles of 0° (for s_{XZ}), 45° (for s_2) or 315° (for s_3) (Fig1A, left panel). In the event a flashed probe was displayed (on 75% of trials), this occurred with equal probability at one of 4 isotropic locations which were 2.5 dva from the fixation dot. Two of these locations were along the radial axis (the axis collinear with the fovea): farther away from fixation ($rad_{fov-out}$), and between the fixation dot and the saccade target (rad_{fov-in}). The other two locations were along the orthogonal (tangential) axis: counterclockwise ($tan_{fov-ccw}$) or clockwise (tan_{fov-cw}) (Fig1A, left panel).

Parafoveal probes condition. The same group of subjects who participated in the foveal condition took part in the parafoveal condition. The location of the saccade targets was the same as in the foveal condition. Here, the probes were presented around the midpoint (at eccentricity of 5°) between the fixation dot and the location of the saccade target (i.e., at the parafoveal retinotopic location mid-way along the saccade trajectory). Each flashed probe appeared 2.5° dva from this parafoveal midpoint along the radial-tangential axes. Specifically, a probe could either be flashed at the inner radial parafoveal location ($rad_{para-in}$) (i.e. location closer to the fovea, which overlaps with the rad_{fov-in} probe location in the fovea experiment), the outer radial parafoveal

location($rad_{para-out}$) (i.e. location further away from the fovea) or along the tangential axis through the parafoveal midpoint either counter clockwise ($tan_{para-ccw}$) or clockwise ($tan_{para-cw}$) (Fig1A, middle panel).

Peripheral probes condition. 5 subjects (2 Males, 3 Females, M_{age}= 25, SD =2.7) were recruited for this condition. With the exception of subject EL (s_{EL}, an author), each subject was completely naïve to the aim of the experiment. Depending on the subject, the saccade target was presented at an eccentricity of 10° with azimuth angles of 270° (for s_1), 315° (for s_2), 0° (for s_3), 45° (for s_4), 90° (for s_{EL}). In this condition a probe was flashed 2.5° dva from the saccade target along the radial-tangential axis. Specifically a flashed probe appeared at either the inner radial location ($rad_{peri-in}$, the same location the $rad_{para-out}$ probe was flashed), the outer radial location ($rad_{peri-out}$), or along the tangential axis either counter clockwise ($tan_{peri-ccw}$) or clockwise ($tan_{peri-cw}$) with respect to the saccade target. (Fig1A, right panel).

Data Analysis

Valid trials. Eye-position and push-button responses obtained from each subject were recorded at 1kHz and stored for further analyses. A trial in which the subject's eye-position landed within the 2-dva tolerance window around the saccade target and within 500ms of the central movement cue was considered a valid trial. Across all subjects we collected a total of 5826 valid trials for the foveal condition, 5579 valid trials for the parafoveal condition, and 9473 valid trials for the peripheral condition.

Saccade onset and offset estimation. For each valid trial, we estimated the onset and offset of the saccade using a "displacement method". Specifically, we calculated the variance in eye-position

before the central movement cue and after the eye landed on the saccade target. We then estimated the lower and upper bounds of the 95% confidence intervals which accounted for any possible *spurious* movement which occurred before and after the saccade. The time points at which the eye-position deviated from these bounds were used to estimate the start (S_{onset}) and end (S_{offset}) of the saccade.

Excluding trial with corrective saccades. We eliminated trials with corrective saccades (i.e., secondary saccades which compensated for under- or overshoots in the primary saccade), since such trials could potentially be associated with non-canonical sensitivity dynamics. Analysis revealed that such trials always had saccade durations (including both the primary and secondary components) greater than 50ms. We therefore eliminated trials with total saccade duration greater than 50ms, and also visually verified that such trials contained a corrective component. In the foveal condition, of the 5826 valid trials, 17 trials were eliminated from subsequent analyses (no-probe =6; $rad_{out-fov}$=3; rad_{fov-in}=3; $tan_{fov-ccw}$=2; $tan_{fov-ccw}$ =3). Similarly, 6 out of 5579 valid trials were eliminated in the parafoveal condition (no-probe =1; $rad_{para-out}$=0; $rad_{para-in}$=3; $tan_{para-ccw}$=1; $tan_{para-cw}$ =1), and 12 out of 9473 valid trials were eliminated in the peripheral condition (no-probe =1; $rad_{peri-out}$=3; $rad_{peri-in}$=3; $tan_{peri-ccw}$=1; $tan_{peri-cw}$ =4).

False alarm rate. We calculated the false alarm as the probability of a button press in trials in which no probe was presented. Subjects performed the task with very low false alarm rates in all experimental conditions: 2%, 1% and 1% respectively in the foveal, parafoveal and peripheral conditions.

Raw fluctuations in sensitivity. To estimate the visual sensitivity at different retinotopic locations during a rapid eye moment, we isolated the valid trials which included a flashed probe at one of the four spatial locations in the foveal, parafoveal and peripheral conditions. We first realigned the trial data to the saccade onset time (time zero) and calculated the probe presentation time with respect to saccade onset. We then calculated sensitivity, separately for the four spatial locations, by using a 25ms sliding window that was moved in 15ms increments. For each time window we calculated the fraction of trials with button pushes over the number of trials in which a probe was presented. To obtain a robust estimate of each subject's sensitivity, we employed a 20-fold jackknife procedure in which the sensitivity was estimated from 95% of the data. This was repeated 20 times, each time leaving out 5% of the data, giving us a mean and error estimate of the sensitivity for each spatial location in each experimental condition ($rad_{fov-out}, rad_{fov-in}, rad_{fov-tcc}, rad_{fov-tcw}$ probes in the foveal experiment; $rad_{para-out}, rad_{para-in}, rad_{para-tcc}, rad_{para-tcw}$ probes in the parafoveal experiment, and the $rad_{peri-out}, rad_{peri-in}, rad_{peri-tcc}, rad_{peri-tcw}$ probes in the peripheral experiment).

Keeping in mind that in the foveal and parafoveal experiment, flashed probes at the rad_{fov-in} and the $rad_{para-in}$ locations, and in the parafoveal and peripheral experiment, flashed probes at the $rad_{para-out}$ and $rad_{peri-in}$ locations were subtended at the same retinotopic location, we further combined the jackknife sensitivity data at these locations. In the same vein, symmetric points along the tangential locations in the foveal, parafoveal and peripheral regions were also combined. Consequently, we obtained a total of seven radial and tangential sensitivity functions: four along the radial axis ($rad_{fov-out}$,rad_{fov-in}+$rad_{para-in}$, $rad_{para-out}$+$rad_{peri-in}$, $rad_{peri-out}$), three along the tangential axes ($tan_{fov-ccw+cw}$, $tan_{para-ccw+cw}$, $tan_{peri-ccw+cw}$) where the x-axis represents the onset of the flashed probes from

saccade onset, while the y-axis represents the sensitivity (percent correct) at a given retinotopic location. To avoid any erroneous sensitivity results due to low sampling, these seven radial and tangential retinotopic functions were truncated over a period from 540ms prior to saccade onset to 130ms after saccade onset. This temporal window included the (i.) pre-planning, (ii.) eye-movement planning, S_{prep}, (computed by taking the temporal difference of S_{onset} from Go_{onset}), and (iii.) execution (S_{onset} to S_{offset}) phases of the cued saccade task.

Normalized sensitivity functions. Despite measuring the CSF at the mean probe location for each experimental condition, it is possible that there are baseline sensitivity differences across probe locations within a condition. To therefore control for any eccentric-dependent effect on the raw sensitivity functions, we normalized these functions by the average sensitivity over the initial 50ms in the data (540ms to 490ms prior to saccade onset).

Periodicity of sensitivity functions. To investigate the frequency components of the sensitivity data, we first de-trended the data by subtracting the mean sensitivity (Supplementary Fig 1B) and then applied a fast Fourier transform (FFT) on the detrended data. To further investigate whether the observed periodicities included a spatial component (i.e., were spatially dependent), we randomly shuffled the probe location identities across experimental trials and calculated the sensitivity function and periodicity of the shuffled data using the same procedures as above. The shuffling procedure was repeated 1000 times for each experiment. Finally, we performed a set of two-tailed paired-sample t-tests between the FFTs calculated from the detrended data and the shuffled data to determine statistical significance.

Time-frequency spectrograms and onset estimation. We applied a multi-taper method on the de-trended data in order to calculate a time-frequency spectrogram [52]. Specifically, we used a single Slepian taper (TW = 3, K = 5) using a sliding window (25ms width, shifted by 25ms). To normalize the time-frequency spectrogram, raw power at each time point was divided by the average power over the time period between 540ms to 500ms before saccade onset. A time-frequency spectrogram was calculated at each of the foveal, parafoveal, and peripheral locations we measured. Finally, we estimated the onset of low-frequency power (3-5Hz) increases at each retinotopic location as the point in time at which low-frequency power reached 90% peak response.

Computational model

Retinotopic mechanics. The purpose of our model was to provide a general mathematical abstraction that reveals the spatiotemporal characteristics, computations and the neural architecture that actively mediates predictive remapping. Our model is agnostic to the specific neural mechanisms that underlie these processes and consists of two basic components: the retinotopic field and a force field (Fig 4A).

Retinotopic field. We refer to the underlying architecture of our model as the retinotopic field (ϕ_r). ϕ_r consists of a two-dimensional hexagonal grid of retinotopic receptive fields - $\mathrm{RF_i}$ - that tile visual space (Fig 4A, small orange circle). Each $\mathrm{RF_i}$ possesses an elastic field – $\mathrm{EF_i}$ (large, dashed orange circle) – which defines the boundary to which it can be perturbed. Consequently, each $\mathrm{RF_i}$ is characterized by three parameters: (a) p_i, the location of the RF center (x_i, y_i) at $\mathrm{t_0}$ (when there is no resultant force acting on the ϕ_r). p_i determines the eccentricity - e_i of $\mathrm{RF_i}$. (b)

s_i, the radius of $\mathrm{RF_i}$ is proportional to e_i. (c) The movement extent (M_{max}) of $\mathrm{RF_i}$ is its $\mathrm{EF_i}$ which is also proportional to e_i.

Force field. Another layer within our model is the force field (ϕ_f). ϕ_f exerts its influence on $\mathrm{RF_i}$ thus causing it to change its p_i at $\mathrm{t_{0+n}}$. Specifically, ϕ_f includes three external forces: the central force ($\overrightarrow{\mathrm{F_C}}$), the peripheral force ($\overrightarrow{\mathrm{F_P}}$), and the translational force ($\overrightarrow{\mathrm{F_T}}$) and an internal force: the equilibrium force ($\overrightarrow{\mathrm{F_E}}$). The external forces are exerted by corresponding time-varying masses: $\mathrm{M_C}$ – the mass subtended on the central region on the retina, $\mathrm{M_P}$ – the mass subtended at a peripheral site, and $\mathrm{M_S}$ – a virtual mass at infinity whose action is to produce a force in the direction of and parallel to the impending saccade. Each mass included the following distributive parts: an exponential growth, a stable plateau, and an exponential decay respectively:

$$\mathrm{M_{plateu}} = \mathrm{M_n e^{t/\tau}}$$

$$\mathrm{M_{plateu}} = \mathrm{M_n e^{(0)}}$$

$$\mathrm{M_{decay}} = \mathrm{M_n e^{-t/\tau}}$$

The following constitutes the possible forces experienced by $\mathrm{RF_i}$ at $\mathrm{t_{0+n}}$:

$$\overrightarrow{\mathrm{F_C}} = \overrightarrow{\mathrm{U_{M_C}}} \,.\, \mathrm{M_c} \,.\, \mathrm{D1_t^{\propto}}$$

$$\overrightarrow{\mathrm{F_P}} = \overrightarrow{\mathrm{U_{M_P}}} \,.\, \mathrm{M_p} \,.\, \mathrm{D2_t^{\propto}}$$

$$\overrightarrow{\mathrm{F_T}} = \overrightarrow{\mathrm{U_{M_S}}} \,.\, \mathrm{M_S} \,.\, |\mathrm{s}|$$

where $\overrightarrow{U_{M_C}}$, $\overrightarrow{U_{M_P}}$, and $\overrightarrow{U_{M_S}}$ are the unit vectors in the direction of the three masses. $D1_t$ and $D2_t$ are the spatial distances between RF_i and M_C or M_P raised to a scalar distance exponent ($\propto$, the principal parameter in our model used to investigate if retinotopic remapping obeys an *inverse distance rule* or a *proportional distance rule,* see Supplementary Fig 1). $|s|$ is the magnitude of the impending saccadic eye movement. A resultant force $\overrightarrow{F_R}$, depending on the simulated condition, could then include a single external force (e.g., $\overrightarrow{F_T}$), two external forces (e.g., $\overrightarrow{F_C}$ and $\overrightarrow{F_P}$), or, in the most dynamic case, all three external forces and the internal force:

$$\overrightarrow{F_R} = k_c \,.\, \overrightarrow{F_C} + k_p \,.\, \overrightarrow{F_P} + k_s \,.\, \overrightarrow{F_T} + \overrightarrow{F_E}$$

where k_c, k_p and k_s are normalizing factors. k_c was obtained by calculating the average of $D1_{t_0}^{\propto}$ across RF_i's and then taking its reciprocal $\frac{1}{|D1_{t_0}^{\propto}|}$. Likewise, k_p was calculated from $D2_{t_0}^{\propto}$. It is worth noting that k_c and k_p were recalculated for a given $\propto$, but once they were obtained were not changed over the time-course of a simulation at t_{0+n}. Furthermore, with k_c and k_p, we obtained a range of magnitude of forces for $\overrightarrow{F_C}$ and $\overrightarrow{F_P}$. With this range, we constructed a look-up table, from which k_s which was selected such that $\overrightarrow{F_T}$ were in the same order of magnitude as $\overrightarrow{F_C}$ and $\overrightarrow{F_P}$. Note that as these external forces exerted their influences on RF_i we calculated $\overrightarrow{F_E}$ as being proportional to the displacement of RF_i (Δd) from its equilibrium position. The simulations were conducted in discrete time increments of 1ms.

Spatiotemporal retinotopic shifts and Density estimation. The time varying forces perturbed each RF_i. To this end, RF_i's movement captured spatiotemporal retinotopic displacements. The concerted movements of the constellations of RF_is manifested in time-varying modulation of

density at a given location of visual space. We modelled each RF_i as a bivariate gaussian kernel function G. To then obtain a probability density estimate, $\hat{f}$, which is equivalent to changes in visual sensitivity in the functional domain, we used the following equation:

$$G\,(u) = \frac{1}{\sqrt{2\pi}} e^{-\frac{1}{2}u^{\mathrm{T}}u}$$

$$\hat{f}\,(\boldsymbol{x}, \mathbf{B}) = \frac{1}{k}\sum_{\mathrm{i}=1}^{\mathrm{k}} \mathrm{G}_{\mathbf{B}}\,(|\boldsymbol{x} - \boldsymbol{x_i}|)$$

Where $\boldsymbol{x_i}$ denotes the spatial co-ordinates of RF_i. B denotes the bandwidth used and was estimated using the recommendation by Bowman and Azzalini [53], with $\mathrm{G}_{\mathbf{B}}$ as a non-negative and symmetric function ($\int G_B(u)du = 1$) defined in bivariate terms as $|\mathrm{B}|^{-1/2}\,G(\mathrm{B}^{-1/2}u)$. Finally, given the eccentric effects we highlighted in our behavioral data, density estimate equivalent to the $rad_{fov-out}$, $rad_{fov+para-in}$, $rad_{para+peri-in}$ and $rad_{peri-out}$ retinotopic locations in all the simulations were normalized by dividing each density estimate by the mean of the first 110ms (i.e. the temporal window within which $\overrightarrow{\mathrm{F_C}}$ is in a steady state).

REFERENCES

1. Helmholtz H.V. Dover; New York, NY: (1962). A treatise on physiological optics.

2. von Holst E, Mittelstaedt H. (1950) The reafferent principle: reciprocal effects between central nervous system and periphery. Naturwissenschaften, 37:464–476.

3. Stark L, Bridgeman B. (1983) Role of corollary discharge in space constancy. Percept. Psychophys ;34:371–380.

4. Medendorp WP. (2011). Spatial constancy mechanisms in motor control. Philos Trans R Soc Lond B Biol Sci 366: 476 – 491.

5. Deubel H, Bridgeman B, Schneider WX. (1998). Immediate post-saccadic information mediates space constancy. Vision Res 38: 3147–3159.

6. Deubel H, Koch C, Bridgeman B. (2010). Landmarks facilitate visual space constancy across saccades and during fixation. Vision Res 50: 249 –259.

7. Duhamel, J.R., Colby, C.L., and Goldberg, M.E. (1992). The updating of the representation of visual space in parietal cortex by intended eye movements. Science, 255(5040), 90–92.

8. Walker M. F., Fitzgibbon E. J., and Goldberg M. E. (1995). Neurons in the monkey superior colliculus predict the visual result of impending saccadic eye movements. J. Neurophysiol. 73, 1988–2003.

9. Sommer M. A., and Wurtz R. H. (2006). Influence of the thalamus on spatial visual processing in frontal cortex. Nature 444, 374–37710.

10. Khayat, P. S., Spekreijse, H., and Roelfsema, P. R. (2004). Correlates of transsaccadic integration in the primary visual cortex of the monkey. Proc. Natl Acad. Sci. 101, 12712–12717.

11. Nakamura, K., and Colby, C.L. (2002). Updating of the visual representation in monkey striate and extrastriate cortex during saccades. Proc Natl Acad Sci. 99(6):4026-31.

12. Tolias, A. S., Moore, T., Smirnakis, S. M., Tehovnik, E. J., Siapas, A. G., and Schiller, P. H. (2001). Eye movements modulate visual receptive fields of V4 neurons. Neuron 29(3), 757-67.

13. Zirnsak, M., Steinmetz, N. A., Noudoost, B., Xu, K. Z., and Moore, T. (2014). Visual space is compressed in prefrontal cortex before eye movements. Nature 507, 504–507.

14. Szinte, M., Jonikaitis, D., Rangelov, D., and Deubel, H. (2018). Pre-saccadic remapping relies on dynamics of spatial attention. eLife 7:e37598.

15. Neupane, S., Guitton, D., and Pack, C. C. (2016). Two distinct types of remapping in primate cortical area V4. Nat. Commun.7:10402.

16. Neupane, S., Guitton, D., and Pack, C.C. (2016b). Dissociation of forward and convergent remapping in primate visual cortex. Curr. Biol. 26, R491–R492.

17. Hartmann, T.S., Zirnsak, M., Marquis, M., Hamker, F.H., and Moore, T. (2017). Two types of receptive field dynamics in area V4 at the time of eye movements? Front. Syst. Neurosci. 11, 1–7.

18. Rayner, K. (1998) Eye movements in reading and information processing: 20 years of research. Psychol. Bull. 124, 372 –422.

19. Wong-Riley, M.T. (2010) Energy metabolism of the visual system. Eye Brain, 2, 99–116.

20. Niven, Jeremy E (2016) Neuronal energy consumption: biophysics, efficiency and evolution. Current Opinion in Neurobiology, 41.129-135.

21. Yao, T., Ketkar, M., Treue, S., and Krishna, B. S. (2016). Visual attention is available at a task-relevant location rapidly after a saccade. eLife, 5 (e18009), 1–12.

22. Chen CY, Hoffmann KP, Distler C, Hafed ZM. (2019) The Foveal Visual Representation of the Primate Superior Colliculus. Curr Biol. 8;29(13):2109-2119.e7.

23. Hafed, Z. M., and Clark, J. J. (2002). Microsaccades as an overt measure of covert attention shifts. *Vision Res*, 42(22):2533-45.

24. Hafed Z.M. (2013). Alteration of visual perception prior microsaccades. Neuron.77(4):775–786.

25. Sperry, R.W., (1950). Neural basis of the spontaneous optokinetic response produced by visual inversion. J. Comp. Physiol. Psychol. 43, 482–489.

26. Sommer, M.A., Wurtz, R.H. (2002). A pathway in primate brain for internal monitoring of movements. Science 296, 1480–1482.

27. Umeno MM, Goldberg ME (1997) Spatial processing in the monkey frontal eye field. I. Predictive visual responses. J Neurophysiol 78:1373–1383

28. Moore T, Armstrong KM (2003) Selective gating of visual signals by microstimulation of frontal cortex. Nature 421: 370–373.

29. Idrees, S., Baumann, M.P., Franke, F., Munch, T.A., and Hafed, Z.M. (2020). Perceptual saccadic suppression starts in the retina. Nat. Commun. 11, 1977.

30. Deubel, H. (2008) The time course of presaccadic attention shifts. Psychol Res, 72(6):630-40.

31. Benedetto, A., Morrone, M.C., (2019). Visual sensitivity and bias oscillate phase-locked to saccadic eye movements. J. Vis. 19, 15.

32. Benedetto, A., and Morrone, M. C. (2017). Saccadic suppression is embedded within extended oscillatory modulation of sensitivity. *The Journal of Neuroscience*, 37 (13), 3661–3670.

33. Hogendoorn, H. (2016). Voluntary saccadic eye movements ride the attentional rhythm. *Journal of Cognitive Neuroscience*, 28 (10), 1625–1635.

34. Fiebelkorn, I.C., Saalmann, Y.B., and Kastner, S. (2013). Rhythmic sampling within and between objects despite sustained attention at a cued location. Current biology: CB 23, 2553–2558.

35. Senoussi, M., Moreland, J.C., Busch, N.A., Dugue, L. (2019). Attention explores space periodically at the theta frequency. J. Vis. 19 (5), 22.

36. Dugué, L., Marque, P., and VanRullen, R. (2015a). Theta oscillations modulate attentional search performance periodically. Journal of Cognitive Neuroscience.

37. Dugué, L., Xue, A. M., and Carrasco, M. (2017). Distinct perceptual rhythms for feature and conjunction searches. Journal of Vision, 17(3):1–15.

38. Castet, E., Jeanjean, S., Montagnini, A., Laugier, D., and Masson, G. S. (2006). Dynamics of attentional deployment during saccadic programming. *Journal of Vision, 6*(3), 196–212.

39. Montagnini A, Castet E. (2007). Spatiotemporal dynamics of visual attention during saccade preparation: Independence and coupling between attention and movement planning. J Vis. 7(14):8.1-16.

40. Levin N, Dumoulin SO, Winawer J, Dougherty RF, Wandell BA. (2010) Cortical maps and white matter tracts following long period of visual deprivation and retinal image restoration. *Neuron*. 65:21–31.

41. Wang, X., Fung, C. A., Guan, S., Wu, S., Goldberg, M. E., and Zhang, M. (2016). Perisaccadic receptive field expansion in the lateral intraparietal area. *Neuron* 90, 400–409.

42. Ross, J., Morrone, M.C., and Burr, D.C. (1997). Compression of visual space before saccades. *Nature* 386, 598–601.

43. Kaiser, M., and Lappe M. (2004) Perisaccadic mislocalization orthogonal to saccade direction. Neuron. 22;41(2):293-300.

44. Deubel, H., Schneider, W.X. (1996) Saccade target selection and object recognition Evidence for a common attentional mechanism. Vision Res; 36: 1827-1837.

45. M. Carrasco, D.L. Evert, I. Chang, S.M. Katz, (1995). The eccentricity effect: Target eccentricity affects performance on conjunction searches. Perception & Psychophysics, 57 (8) 1241-126.

46. Melcher D, Colby CL (2008) Trans-saccadic perception. Trends Cogn Sci 12:466–473.

47. Melcher, D. (2007) Predictive remapping of visual features precedes saccadic eye movements. Nat. Neurosci. 10, 903–907.

48. Mays L.E., Sparks DL. J. (1980) Dissociation of visual and saccade-related responses in superior colliculus neurons. Neurophysiol. 43(1):207-32.

49. Goldberg ME, Bruce CJ. Primate frontal eye fields. III. (1990) Maintenance of a spatially accurate saccade signal. *J Neurophysiol* 64: 489–508.

50. Rolfs, M., Jonikaitis, D., Deubel, H., and Cavanagh, P. (2011). Predictive remapping of attention across eye movements. Nat. Neurosci. 14, 252–256.

51. Jonikaitis D, Szinte M, Rolfs M, Cavanagh P. (2013). Allocation of attention across saccades. Journal of Neurophysiology. 109:1425–1434.

52. Bokil, H., Andrews, P., Kulkarni, J.E., Mehta, S., Mitra, P.P. (2010) Chronux: A platform for analyzing neural signals. J Neurosci Methods192:146–151. 54.

53. Bowman, A. W. and Azzalini, A. (1997). Applied Smoothing Techniques for Data Analysis: the Kernel Approach with S-Plus Illustrations. Oxford University Press, Oxford.

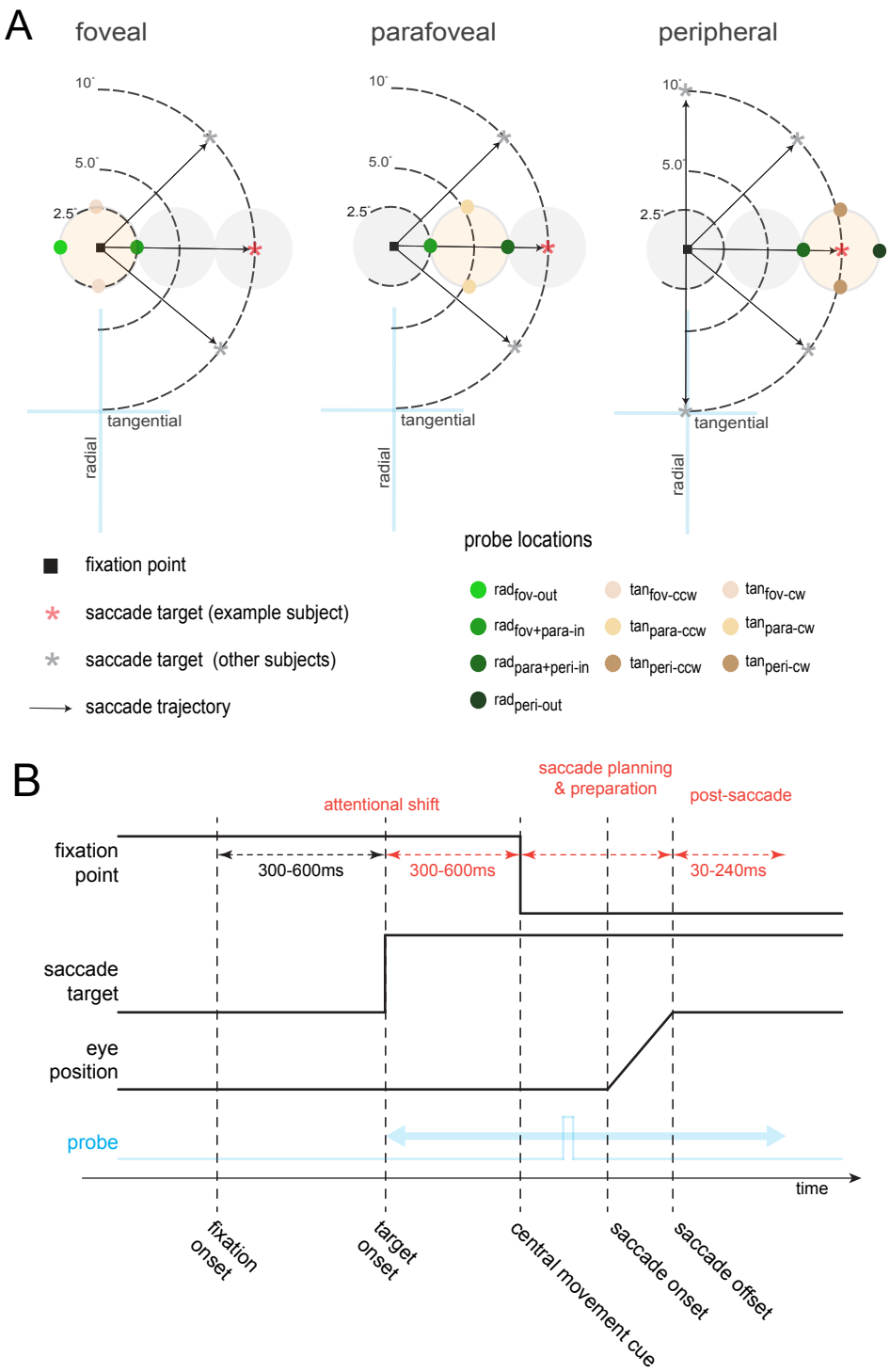

Figure 1. Peri-saccadic probe-detection task.
(A) Spatial locations tested across experiments. Colored circles show the locations at which a low-contrast probe was flashed as subjects planned and prepared a saccade (black arrow) towards the periphery. Probe locations are shown only for horizontal saccades to the right. For other saccade target locations, the probe locations were appropriately positioned along and around the path of a saccade. In the foveal and parafoveal experiments, a saccade target (gray or red asterisk) was presented at azimuth angles of 0°, 45°, 315° (each subject had a different angle). In the peripheral experiment the saccade target was presented either at azimuth angles of 0°, 45°, 90°, 270°, 315° (each subject had a different angle).
(B) Temporal sequence of an example trial. The start of a trial began with the appearance of a fixation-point, followed by a time-varying presentation of the saccade target. A low-contrast probe was flashed either before the onset of the central movement cue (the pre-saccadic condition), or after (the post-saccadic condition).

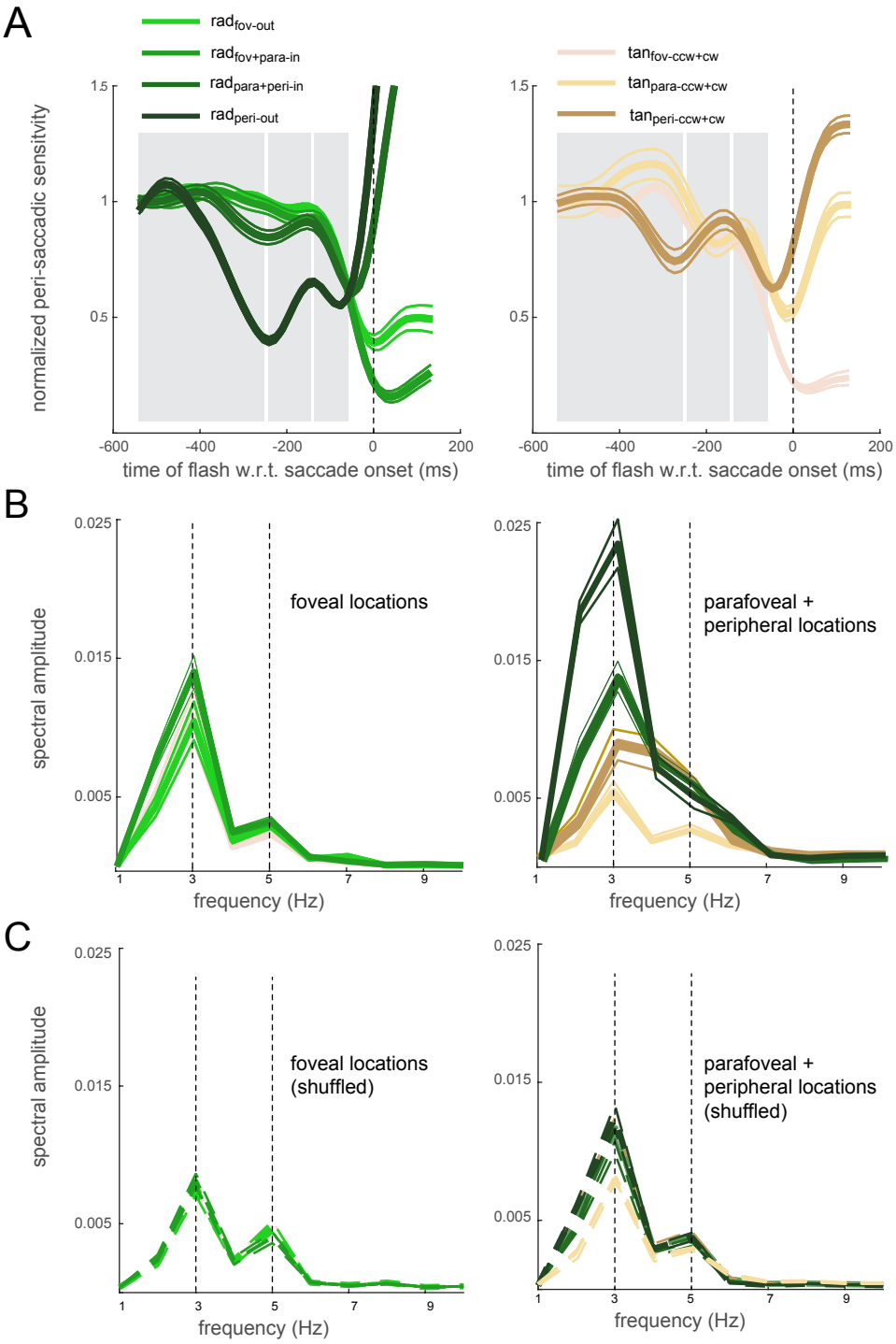

Figure 2. Peri-saccadic sensitivity functions and their frequency domain representation across visual space.
(A) Thick solid lines represent normalized changes in peri-saccadic sensitivity as a function of flashed probe times relative to saccade onset along and around the saccade trajectory (n=11). The thin lines represent corresponding error estimates obtained using a 20-fold jackknife procedure in which the sensitivity was estimated from 95% of the data.
(B) Frequency domain representation of detrended peri-saccadic sensitivity. The thinner solid lines represent the error estimates calculated across subjects.
(C) Frequency domain representation of shuffled peri-saccadic sensitivity data (n=1000).

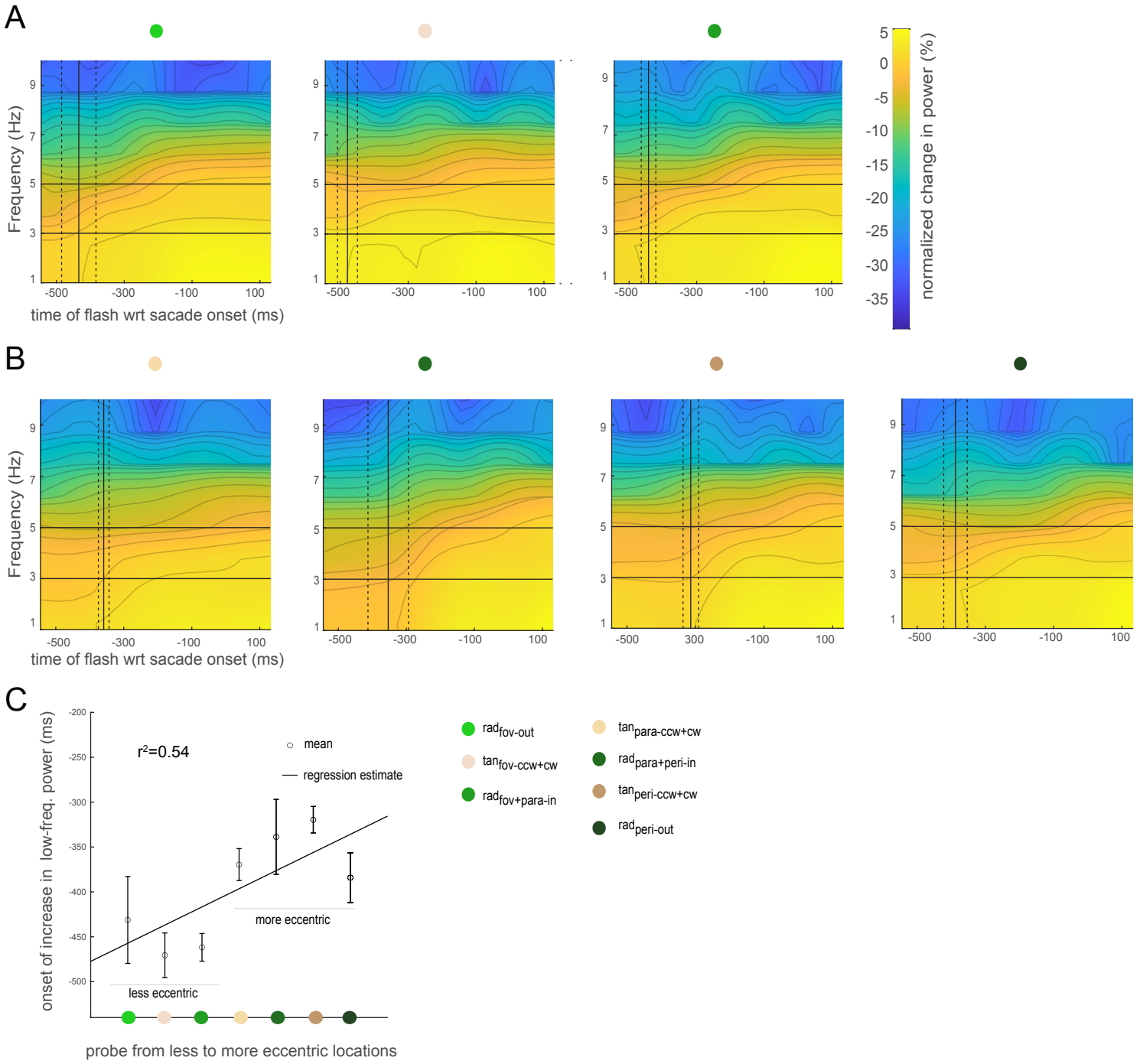

Figure 3. Time-frequency spectrograms across visual space during peri-saccadic probe-detection task.
(A) Time-frequency spectrogram at the less eccentric (foveal) locations. The vertical solid lines represent onset of increase in low-frequency power, while the vertical dashed lines represent the error estimates. The solid horizontal lines represent the low-frequency power range from 3 to 5 Hz.
(B) Same as in (A) at the more eccentric (parafoveal and peripheral) locations.
(C) Estimation of onsets of increases in low-frequency power around and along the path of a saccade. Onset estimates were fitted with a linear regression line. Onset time increased as the spatial location being sampled became more eccentric. Error bars indicate standard error of the mean.

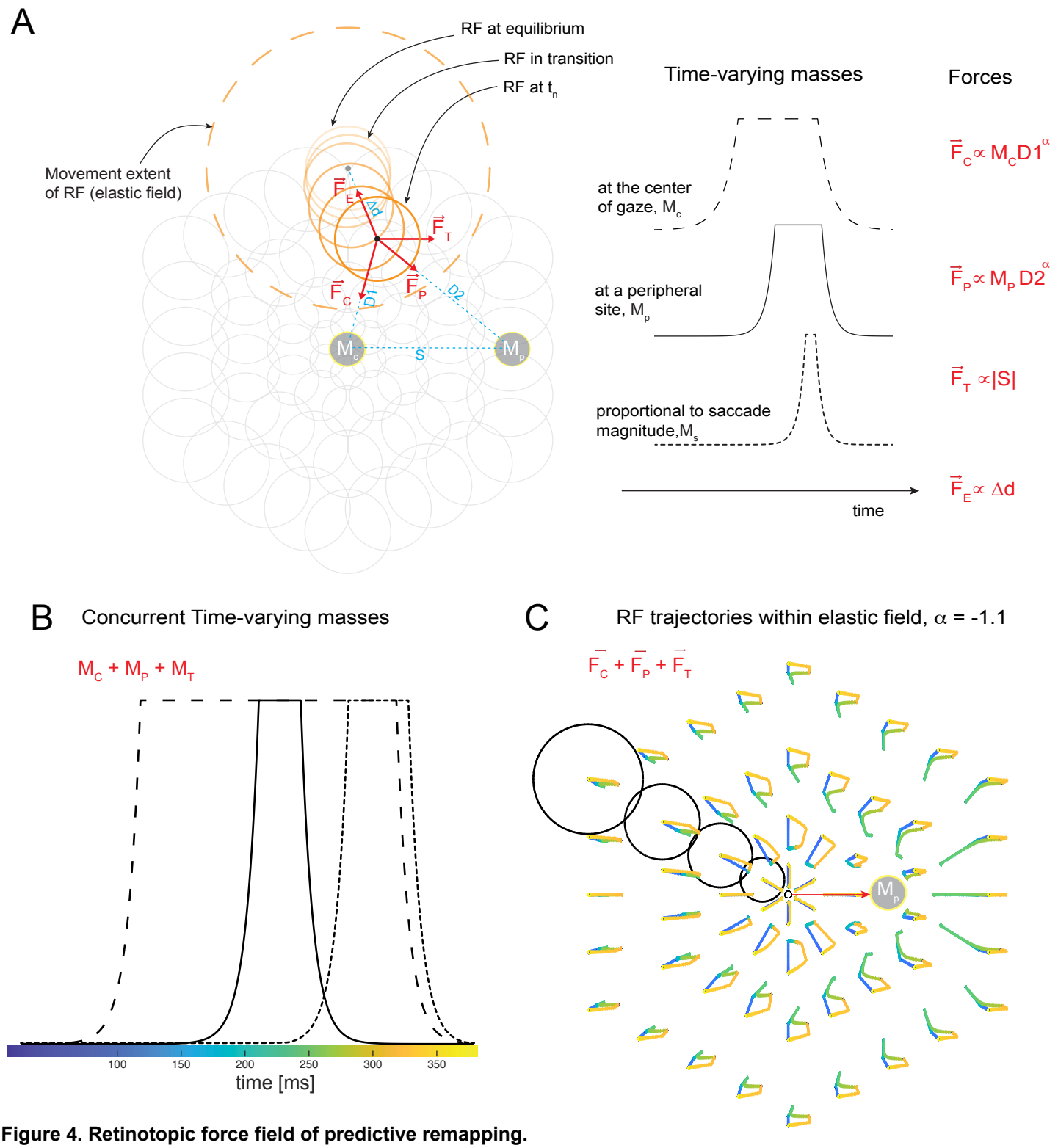

Figure 4. Retinotopic force field of predictive remapping.
(A) Retinotopic field consisting of population receptive field (pRFs) that tile visual space. For illustration purposes, a single pRF is highlighted in orange. This pRF is characterized by the location of its center at equilibrium (gray dot), its size (orange circle) and a movement extent (elastic field, pEF; dashed orange circle). Both pRF size and pEF extent are eccentricity dependent. M_C represents compressive signals and is modelled as a varying mass located at the center of gaze. M_P represents convergent signals and is modeled as a varying mass located at the peripheral site corresponding to the saccade target. M_T represents translational signals and is modelled as a virtual mass at infinity located in the direction of the impending saccade.
(B) Temporally overlapping varying masses for the case when pRFs were perturbed by a combination of all three independent forces.
(C) Corresponding spatiotemporal pRF trajectories under an inverse force field (α=-1.1). Note that each pRF possess an eccentricity dependent pEF, however for illustration purposes only a few are shown (black circles). The trajectories are color coded as in (B).

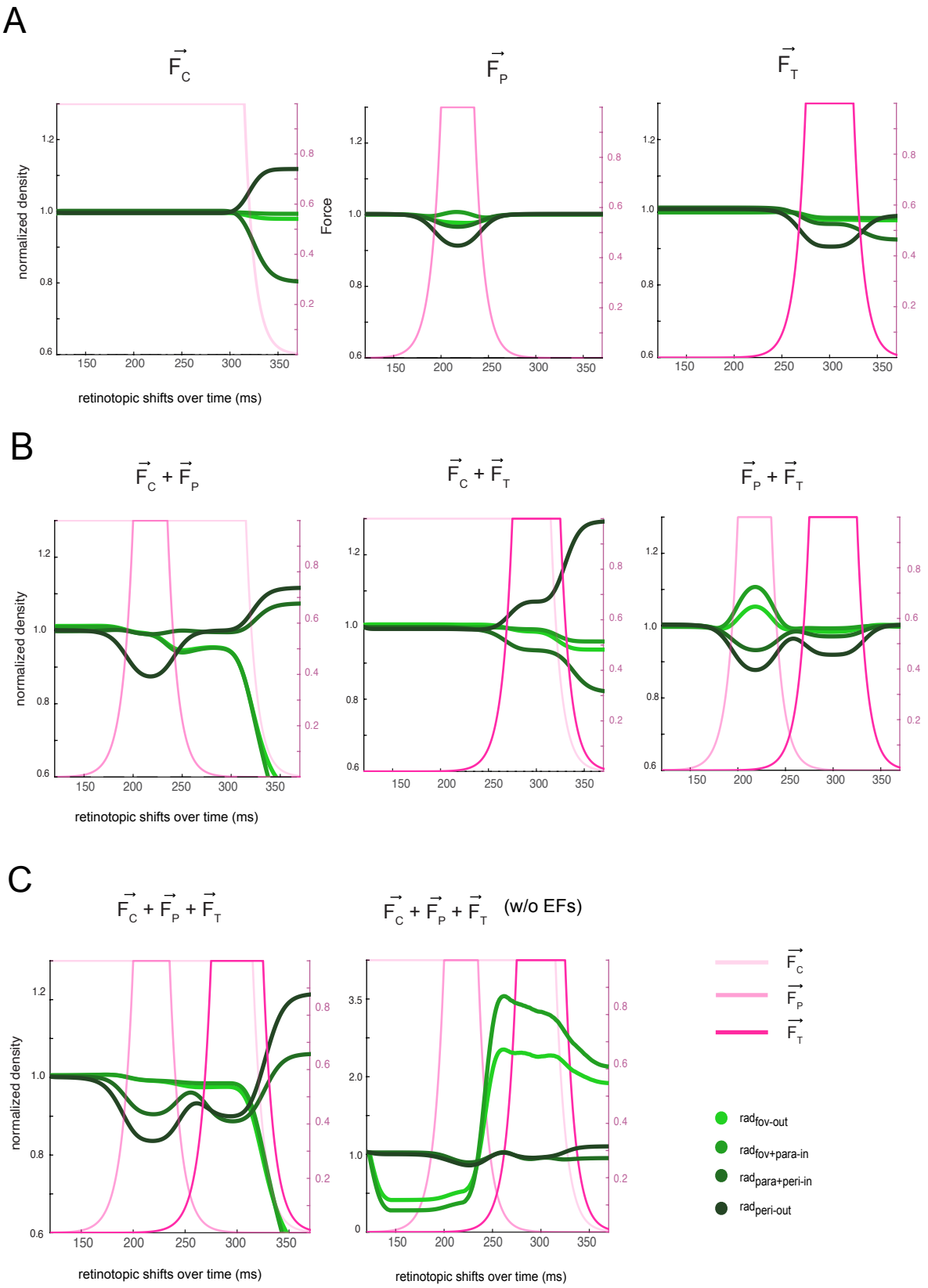

Figure 5. Temporally overlapping compressive, convergent and translational shifts explain peri-saccadic changes in sensitivity across visual space. Simulation results at α=-1.1 in cases when pRFs are perturbed by (A) a single external force (B) two external forces and (C) three external forces. The right panel in (C) are the results for the three force simulations without elastic fields. Along the right y axis is the magnitude of the time varying masses used to model putative signals to the retinotopic field, while the x-axis represents the simulation time sampled at discrete increments of 1ms.